On-road vehicle aerodynamics with a large-scale stereoscopic-PIV setup "the Ring of Fire"

Hüttig, Steffen; Kühn, Malte; Gericke, Timo; Bloem, Guus; Sciacchitano, Andrea; Akkermans, Rinie A.D.

DOI
10.1007/s00348-025-04025-w

Publication date
2025

Document Version
Final published version

Published in
Experiments in Fluids

Citation (APA)
Hüttig, S., Kühn, M., Gericke, T., Bloem, G., Sciacchitano, A., & Akkermans, R. A. D. (2025). On-road vehicle aerodynamics with a large-scale stereoscopic-PIV setup: "the Ring of Fire". *Experiments in Fluids*, *66*(6), Article 125. https://doi.org/10.1007/s00348-025-04025-w

Experiments in Fluids (2025) 66:125
https://doi.org/10.1007/s00348-025-04025-w

REVIEW

On-road vehicle aerodynamics with a large-scale stereoscopic-PIV setup: "the Ring of Fire"

Steffen Hüttig[1,2] · Malte Kühn[1] · Timo Gericke[1] · Guus Bloem[3] · Andrea Sciacchitano[3] · Rinie A. D. Akkermans[4]

Received: 29 April 2024 / Revised: 21 March 2025 / Accepted: 24 March 2025

Abstract

This paper presents the first full-scale particle image velocimetry (PIV) measurements to analyze the flow field of a car under real driving conditions. The Ring of Fire (RoF) measurement concept, introduced by Terra et al. (Exp Fluids 58:83, 2017. https://doi.org/10.1007/s00348-017-2331-0), is adapted to automotive demands to validate CFD simulations for further improvements of vehicle aerodynamics. The experiment consists of a tunnel setup, where neutrally buoyant helium-filled soap bubbles are used as flow tracers and are illuminated by two high-speed lasers. Four high-speed cameras captured the particles motion in two separate Stereo-PIV configurations with fields of view of $1.3 \times 0.6\ \mathrm{m}^2$ and $2.8 \times 2.2\ \mathrm{m}^2$. Data for a Volkswagen up!, while driving on a test track at a constant speed of 33.33 m/s, was acquired for the wake and the side mirror region and processed with standard multi-pass PIV algorithms, in order to quantify the flow field and estimate limits of the described measurement principle for on-road car aerodynamics. The resulting ensemble averaged velocity fields are compared with CFD simulations, showing agreement for the here considered cases within 7.0–9.7%, based on the root-mean-square error between the experimental and the numerical results. Furthermore, drag calculation from the obtained velocity fields based on moment conservation is performed and the percent difference to wind tunnel measurements reaches values below 3.0%.

Graphical abstract

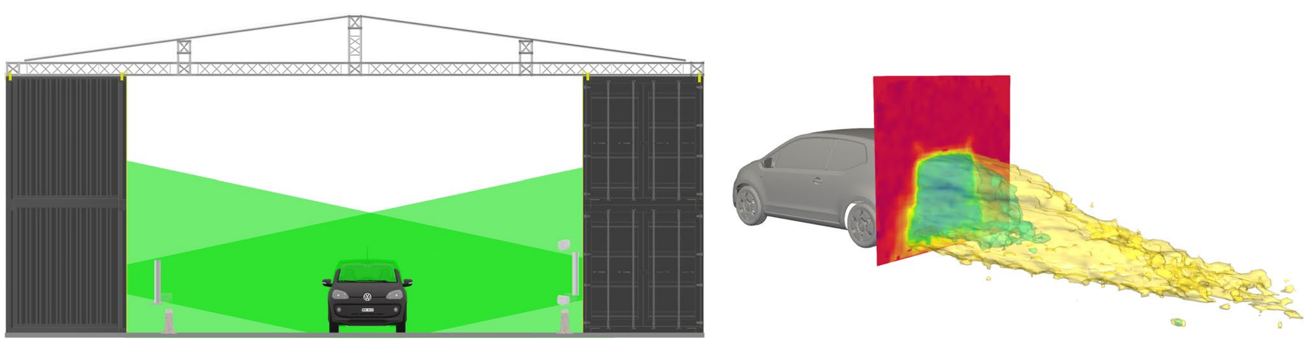

1 Introduction

The aerodynamic optimization has and will be one of the main focuses in the design and development of cars, not only to achieve aerodynamic drag reduction and therefore additional range, but also to enhance the car performances with respect to other topics such as soiling (e.g., rain, dust and snow), aeroacoustics (e.g., exterior side mirror (Dawi and Akkermans 2018)) or with the further development of autonomous driving technology and the adaptation of legislation vehicles in a platoon configuration (Ebrahim and Dominy 2021). Most experimental aerodynamic investigations are performed in large automotive wind tunnels under controlled and reproducible conditions, where, for instance, drag analysis is performed via the measurement of aerodynamic forces with a balance connected to the vehicle. The rotation of the wheels is implemented by a roller or flat belt dynamometer and moving ground is usually simulated by a conveyor belt in the middle of the car. Both measures aim to mimic real on-road conditions; however, several factors

Extended author information available on the last page of the article including the presence of the model supports, the low turbulence intensity of the inflow and the difficulty to simulate the car motion along a curvilinear path, preclude reproducing the on-road conditions realistically. Flow field quantification around a vehicle is usually performed with Pitot rakes, e.g., Jones (1936), pressure taps or rakes or hot-wire anemometry (Perry 1982) where the latter has a high-frequency response (up to several hundreds of kHz) with the capabilities to resolve high-frequency velocity fluctuations. All the listed techniques, however, are characterized by low spatial resolution and need to be traversed or mounted in various positions to achieve a quantification of the car wake in a volume. In contrast, particle image velocimetry (PIV) is established to instantaneously quantify flow fields and the flow velocity components in a nonintrusive manner; furthermore, with the introduction of neutrally buoyant helium-filled soap bubbles (HFSBs) by Bosbach et al. (2009) as tracer particles, the maximum field of view (FOV) can be extended to several square meters.

On-track flow quantification has been conducted by various authors (see, e.g., Schröck (2012); Watkins et al. (1990); Stoll (2018); Jessing (2021)) with the aim to resolve the effects of different flow conditions like crosswind, traffic or even topography. The aforementioned experiments were conducted with the use of surface mounted pressure probes or different rakes to resolve the pressure distribution at different locations, however, with limited spatial resolution. First full-scale PIV measurements of the flow between the underfloor of a passing high-speed train were performed by Henning et al. (2016). On-road flow quantification with vehicle mounted setups was performed by Haff (2015) for flow analysis of the near wake of a tractor-trailer heavy-duty vehicle and by Haff et al. (2017) to resolve underbody flow fields of a passenger car. However, the aforementioned experiments were performed with the use of sub-micrometer particles, which limited the possible field of view to a maximum of approximately 0.8×0.8 m^2.

With the introduction of the Ring of Fire measurement concept by Terra et al. (2017) in 2017, the beneficial light scattering characteristics of HFSB were used to resolve the whole wake of road cyclists under on-site conditions by Spoelstra et al. (2018). In contrast to normal wind tunnel tests, the frame of reference is changed, with an object moving at constant velocity through stagnant air. From the ensemble averaged measured velocity fields, the aerodynamic drag was evaluated using the conservation of momentum applied to a control volume around the moving model ((Spoelstra et al. 2018, 2019, 2023)).

To the best of the authors' knowledge, the application of the Ring of Fire concept to on-road automotive situations has not been attempted before; hence, the present work describes the realization of this concept for real driving car aerodynamics analysis. The goal was to evaluate the capabilities and challenges of this flow field quantification technique for automotive demands. In this work, results of a small hatchback Volkswagen up! are presented. This car was used since it was equipped with pressure tabs from previous investigations; also, a wide range of flow field information from CFD is available.

The experimental setup will be explained in Sect. 2, followed by the conducted data processing in Sect. 3. Results of the flow field around a car mirror and in the wake of the car are discussed and compared to the CFD-Data in Sect. 4. Finally, the conclusion is presented in Sect. 5.

2 Experimental setup—Ring of Fire

The large-scale PIV measurements were conducted in August and September 2021 at the Volkswagen proving ground in Ehra-Lessien (Germany). The measurements were performed during the night, to minimize the undesired effects from the ambient wind. The setup consists of a tunnel-like construction built of eight shipping containers and roof construction of trusses and a tarp. Further containers were used for storage of the equipment and a dedicated control room, as illustrated in Fig. 1.

The construction was set up at a straight track with a total length of 950 m. The test section was placed at a location 685 m after the starting position, resulting in a sufficient distance for the acceleration, constant speed and breaking of the vehicles, see Fig. 2.

Two cars were used during the measurement campaign to investigate the flow field, with the aim to show the potential of the measurement setup to visualize and quantify the large flow structures under real driving conditions. In this publication, results of the Volkswagen up!, also used for previous on-road experiments by Placzek (2018), are shown. The car is equipped with 200 surface pressure taps. The test vehicle was wrapped/painted black in order to reduce reflections of the laser light. Only the windscreen and front side windows were kept uncovered to enable the driver to see the road (see Fig. 3a)). Two regions of interest for the measurements were considered, namely the region around the side mirror and the car wake, as illustrated in Fig. 3b).

Velocity measurements in the two regions (wake & close-up FOV) were acquired simultaneously with two large-scale stereoscopic-PIV systems. For the wake analysis, two Photron SA-X2 cameras (Camera 1 & 2 in Fig. 1) were placed at the tunnel entrance, with a distance of 7.6 m to the light sheet. Both cameras were equipped with LaVision Scheimpflug-Adaptors v3 and Nikon Nikkor lens with a focal length of $f = 60$ mm. For the close-up region, two Phantom cameras v2011 & v1611 were placed on top of each other on the left side of the road with a distance of 4.3 m behind the light sheet. The cameras were equipped

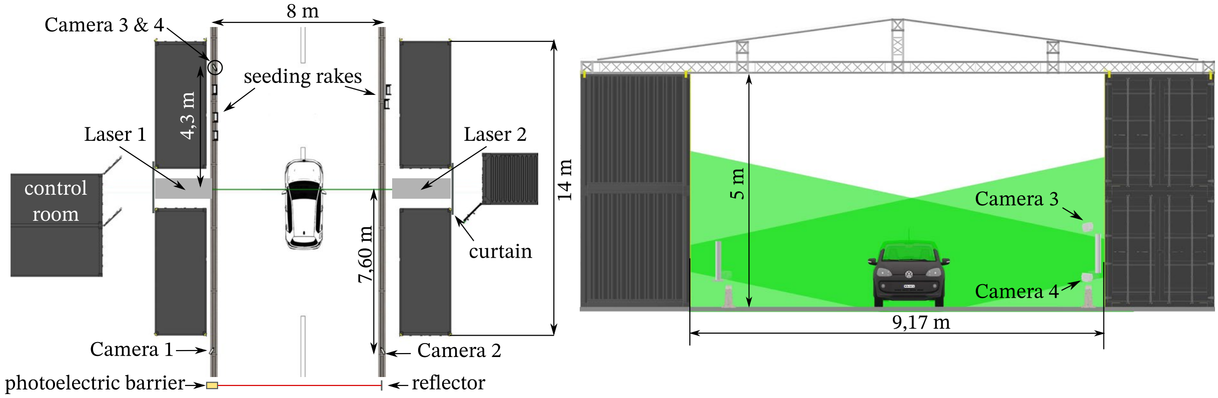

Fig. 1 Schematic setup and position of experimental hardware. (left) top view and (right) front view with Volkswagen up! partly passing the laser sheet

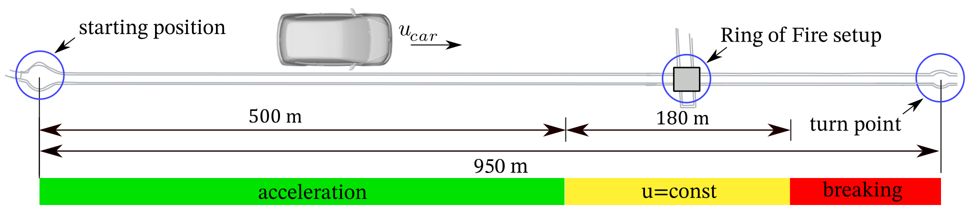

Fig. 2 Track dimensions and position of experimental measurement

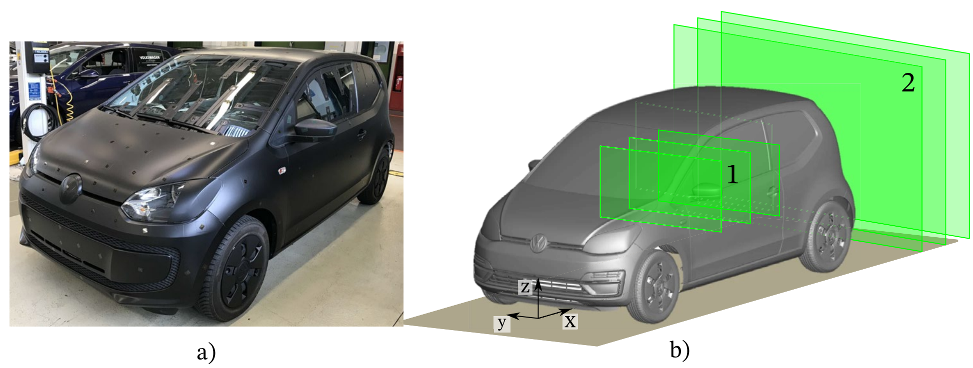

Fig. 3 **a** Actual test vehicle: Volkswagen up!; **b** corresponding regions of interest

with Scheimpflug-Adaptors v4.2 from LaVision and Sigma MAKRO lenses with a focal length of $f = 180$ mm. Illumination was realized by two Quantronix High-Speed Lasers (Hawk Pro & Hawk II), equipped with light sheet optics, one at each side of the road, placed in between the containers.

To contain tracer particles close to the measurement plane, the tunnel structure was built on the test track with an asphalt width of 8 m. The tunnel was 14 m long, 9.17 m in width and 5.3 m in height, yielding a blockage ratio of 4.3 % for the Volkswagen up!, see Fig. 1. To ensure the safety within the measurement area, safety barriers (Delta-block DB50SL) were installed on each side with a length of 120 m. Furthermore, the driver was equipped with a pair of laser goggles for eye safety.

Neutrally buoyant helium-filled soap bubbles were used as tracer particles. They were introduced in the measurement area by 14 20-nozzle LaVision seeding array and a 204-nozzle-generator seeding rake (composed of 12 wings with 17 generators each) from TU Delft, producing in total up to 18 million bubbles per second. Two LaVision fluid supply units (FSU) controlled the soap, air and helium flow rates toward the seeding rakes on each side of the road (see Fig. 1). The rakes were placed on X-95 beams along the track for a quick repositioning according to the daily ambient conditions. In order to maintain the seeding in the test section, the gap between the containers was closed by the use of curtains, which also provided the necessary laser safety for the environment. An overview of the used equipment is given in Table 1.

Table 1 Overview of Equipment parameters

Purpose	Instrument	Region of interest	
		Mirror	Wake
Imaging	Cameras	Phantom v1610 & v2011 CMOS, 35.8x22.4 mm^2 1280×800 pixels pixel pitch 28 µm, 12 bits	2× Photron Fastcam SA-X2 CMOS, 20.48×20.48 mm^2 1024×1024 pixels pixel pitch 20 µm, 12 bits
	Lenses	2× Sigma MAKRO f=180 mm	2× Nikon Nikkor f=60 mm
	Others	2× LaVision Scheimpflug v4.2	2× LaVision Scheimpflug v3
	Trigger	Eltima Electronic - Joker^2 light barrier system	
Calibration	3D-Calibration plate	1440×1440×60 mm^3 plane to plane distance 20 mm 18×18 markers per plane Ø=8 mm ; marker spacing = 80 mm	
Illumination	Laser	Quantronix Hawk Pro and Hawk II Nd: YAG 523 nm 2×6 mJ at 6 kHz	
Seeding	Tracer particles	Helium-filled soap bubbles	
	Seeding system	2× LaVision Fluid Supply Unit 14× LaVision 20 nozzle array 1× TU Delft 204 nozzle seeder	

2.1 Test procedure

Measurements took place during August and September 2021 and were conducted at night times, since the ambient flow tends to settle down after the sunset, thereby reducing the wind speed. Each day the hardware was stored in the storage containers to protect it against humidity and possible rain; lasers and cameras were mounted and calibrated at the beginning of each measurement day. Before the first run, the cars cruise control velocity was set to 33.33 m/s with a digital GPS-Speedometer and saved; thus, the same speeds (standard deviation SD = 0.183 m/s) were reached each run by the use of the resume function of the cruise control. In order to enhance the repeatability of the measurements, only one driver drove the cars for the whole campaign. To accumulate a sufficient amount of seeding particles within the measurement volume, two tarps were installed during the experiment at the entrance and exit of the tunnel (see Appendix A left container side); depending on ambient wind direction, one was closed for filling the tunnel with HFSB for approximately 5 min, while the car would drive to the starting position. The supporting scientists observed the seeding density and ambient flow conditions and gave the starting signal via radio, once sufficient seeding had been accumulated. In order to maintain enough HFSB in the test section, the curtain was kept closed until the driver gave a signal, whereupon the curtain was opened. DaVis 10.2.0 was used for synchronizing the hardware and the image acquisition, which was triggered by a photoelectric sensor. Images were acquired at 6 kHz in continuous mode, which, at a car velocity of u_{car} = 33.33 m/s (120 km/h),

Table 2 Overview of imaging and acquisition parameters

Purpose	Parameter	Region of interest	
		Mirror	Wake
Field of view	x (thickness) [cm]	3.5–5	3.5–5
	y (width) [m]	1.3	2.8
	z (height) [m]	0.6	2.2
Imaging	$f_\#$	4.0	4.0
	Magnification	0.032	0.008
	Object distance [m]	5.36	8.6
	Image resolution [mm/px]	0.38	2.63
	Stereoscopic angle	23°	50°
Measurement rate	f_{acq} [Hz]	6000	6000
Seeding concentration	particle image density [ppp]	0.005–0.01	0.009–0.025

corresponds to a measurement every 5.55 mm displacement of the car. The imaging and acquisition parameters are described in Table 2.

A total of 6000 images (1 s acquisition time, corresponding to a displacement of the car of 33.33 m) were saved for each run, with the first frame 167 ms before the car entered the light sheet. During the transfer of the data from the internal camera memory to the computer, the car returned to the starting position and the tunnel was filled with HFSB again. The vehicle's ride height has a large influence on the total drag and was measured for each run by means of a fifth high-speed camera mounted at the side of the road with a FOV at the wheel and fender of the car. Defined markers on the car allowed the scaling of the recorded images and thus measurement of the ride height, to assure constant conditions for the averaged drag calculations. These results are discussed in Sect. 4.3.

3 Data processing

The presented two Stereo-PIV image sets (wake and mirror regions) required different processing steps due to the different camera types and FOV. In both cases, a planar self-calibration from Wieneke (2005) was applied on images in front of the car with good seeding density and distribution.

3.1 Car wake analysis

For the wake analysis and drag calculation, each measurement was separated into two parts. The first one included the first 100 images about 5.5 meters in front of the car to determine the ambient flow. The second part included 1800 frames (10 m car displacement) behind the car for the wake analysis. Background subtraction of an average of 100 images was used to reduce reflections of all objects (e.g., background & light sheet (stationary) and car body (quasi-stationary)). Furthermore, a sliding background subtraction and a min/max-filter, each in space and with a filter length $L = 4$pixels, as well as a geometric mask, were applied. Sample raw and preprocessed images are shown in Fig. 4.

The displacement vector determination was performed by the sliding sum-of-correlation approach (1st pass: window size 64×64, square weighting, 50 % overlap; 2nd to 4th pass: window size 48×48, Gaussian weighting, 75 % overlap) introduced by Sciacchitano et al. (2012) with a kernel length of $L = 7$ frames and a time interval of $3\times \Delta t_0 = 0.5$ ms; thus the resulting velocity field was calculated over 16 image pairs and Gaussian weighted, which has shown to improve the correlation results by Beresh et al. (2021).

Post-processing was performed by the universal outlier detection (Westerweel and Scarano (2005)) within a kernel of 5×5 vectors. Linear interpolation was used to fill in empty spaces caused by the outlier removal. The phase-averaging of in total 32 runs region 1 and 22 runs region 2 with sufficient seeding density had to take into account that the car passed in each run at a different lateral position (up to 20 cm left to right). This was resolved by the use of a distinct marker on the car and a resulting correction of the coordinate systems origin for each run.

3.2 Mirror and A-pillar analysis

For the mirror and A-pillar analysis, a total of 800 frames, corresponding to a car displacement of 4.4 m, respectively, a range of $x/h = [-0.5;2.5]$, were processed for a total of 32 runs. Beside the conversion from RGB to gray scale, the directional minimum filter with a filter length of $L = 5$ pixels was used to reduce background noise and unsteady reflections. Furthermore, a dynamic masking method was introduced, since the object moved through the image plane and therefore a different mask had to be applied for each frame.

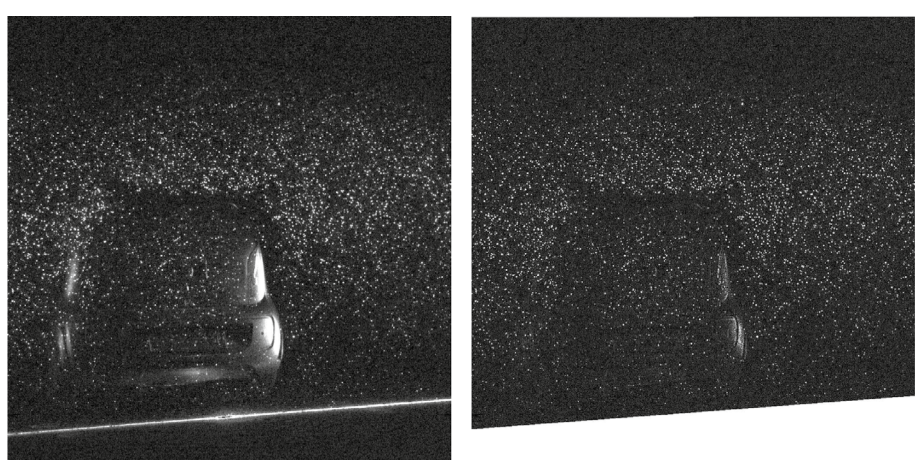

a) b)

Fig. 4 Samples of an image recording for the car wake measurements: **a** raw and **b** preprocessed image with background subtraction and applied mask

The first step is the correct mapping of the image coordinate system to the car coordinate system by the use of markers on the car. With this information, a corresponding slice of a CAD-model is taken at the same x-position of the car and the resulting edge of the body was used to define the mask. Afterward, the mask was transferred into the camera coordinate system by the use of the calibration information of DaVis and finally applied to each individual image. An example of the processing steps is displayed in Fig. 5.

The vector calculation was also performed with the sliding sum-of-correlation approach (1st pass: window size 128×128, uniform (top-hat) weighting, 50 % overlap; 2nd to 5th pass: window size 48×48, adaptive weighting, 75 % overlap; kernel length of $N = 6$ frames), followed by vector post-processing with the aforementioned universal outlier detection within a kernel of 5×5 vectors. In order to resolve the highly turbulent flow in the wake of the mirror and to fulfill the 1/4-rule of the out-of-plane velocity introduced by Keane and Adrian (1991), the frames were processed with a time separation of $\Delta t_0 = 166.37\ \mu s$, corresponding to the acquisition frequency of 6 kHz. The averaging of the 32 runs made use of the positioning information of the masking procedure to correct for the different lateral positions of the car. A linear interpolation of the velocity fields was applied to map the velocity vectors onto the same grid. The number of used runs differs from the number of runs for the wake analysis due to different seeding quality in the two fields of view.

Because of the relatively large laser sheet thickness (about 5 cm) and the highly turbulent flow in the wake of the side mirror, the cross-correlation-based interrogation algorithm detects multiple displacement peaks of similar heights (see Fig. 6), thus leading to an erroneous evaluation of the average particle image displacement. Therefore, only the flow field upstream of the A-pillar and side mirror will be further discussed in Sect. 4.1. An overview of the processing parameters of both regions of interest is given in Table 3.

3.3 Drag calculation

In recent years, the Ring of Fire system has been used to evaluate the drag of transiting objects such as spheres, cyclists and ice skaters (Terra et al. (2017); Spoelstra et al. (2019, 2021); Terra et al. (2023)). The drag was computed by applying the conservation of momentum (Mohebbian and Rival (2012)) in a control volume enclosing the transiting object. The control volume is selected such that there is no mass and momentum flow across the side, top and bottom faces, leaving only the inlet and outlet plane for the net momentum flow. Furthermore, unsteady contribution to the drag force can be neglected, since the car has a fixed geometry and moves at a constant speed. Moreover, due to the high Reynolds number of 3.30 x 10^6 based on the vehicle height, the contribution of the viscous effects is also negligible (Kurtulus et al. (2007)), leaving Eq. 1 for the instantaneous aerodynamic drag. The application of Eq. 1 requires that the mass flow through the inlet plane S_{inlet} is the same as that through the outlet plane S_{outlet}. To apply this

Fig. 5 Samples of an image recording for the car mirror measurement **a** raw image; **b** CAD-model and extracted mask (purple); **c** preprocessed image converted to gray scale and masked

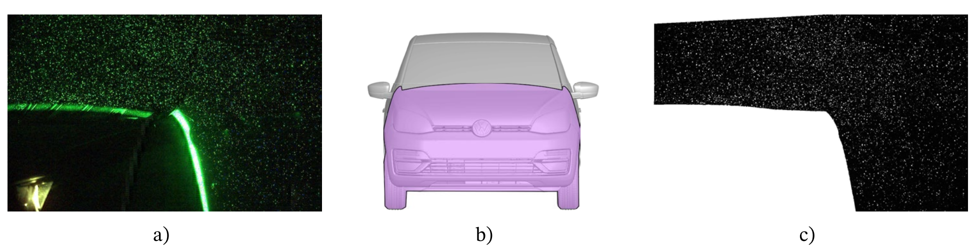

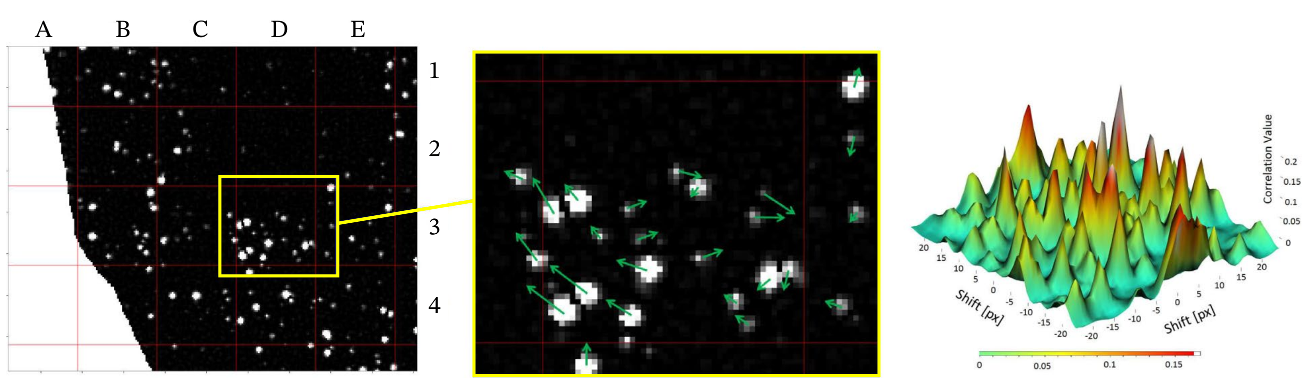

Fig. 6 Seeding distribution and resulting correlation peak in the wake of the side mirror

Table 3 PIV-processing parameters

Parameter	Mirror & A-Pillar	Car Wake
Correlation algorithm	Sliding sum-of-correlation	Sliding sum-of-correlation
Interrogation windows overlap factors	1st pass 128×128 pixel 75 % overlap–uniform weighting 2nd-5th pass 48×48 pixel (40×40 mm^2) 50 % overlap–adaptive weighting	1st pass 64×64 pixel 75 % overlap–uniform weighting 2nd-4th pass $\times 48 \times 48$ pixel (126×126 mm^2) 75 % overlap–Gaussian weighting
Vector pitch	10 mm	32 mm
Dynamic spatial range	33	23
Dynamic velocity range	242	282

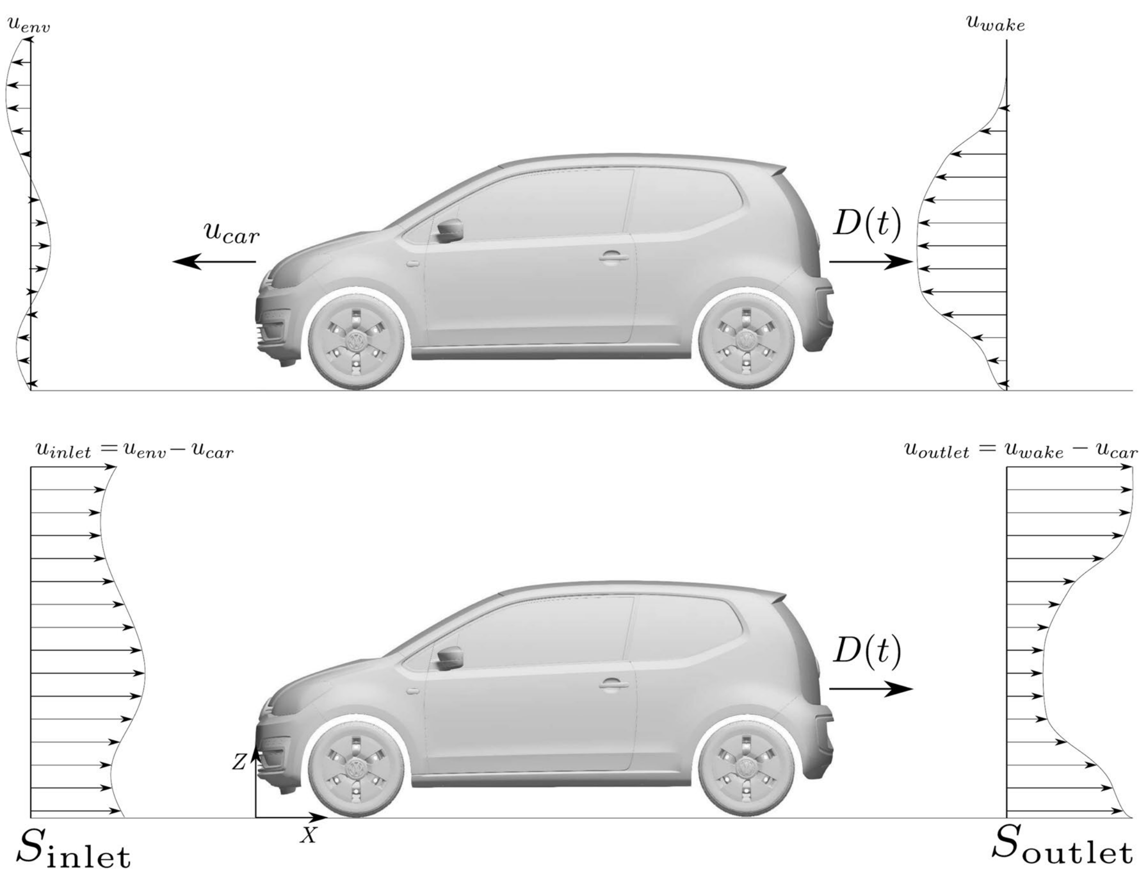

Fig. 7 Galilean transformation from static to moving frame of reference, adapted from Spoelstra et al. (2019)

equation, the Galilean transformation from a static to a moving frame of reference is performed, where the car's velocity is subtracted from the measured velocities, as illustrated in Fig. 7. Here, u_{env} is the streamwise velocity component measured at the inlet, i.e., before the passage of the car. As opposed to this, u_{wake} is the streamwise velocity component measured after the passage of the car.

$$D(t) = \rho \iint_{S_{\mathrm{inlet}}} (u_{env} - u_{\mathrm{car}})^2 \, dS - \rho \iint_{S_{\mathrm{outlet}}} (u_{\mathrm{wake}} - u_{\mathrm{car}})^2 \, dS + \iint_{S_{\mathrm{inlet}}} p_{\mathrm{inlet}} \, dS - \iint_{S_{\mathrm{outlet}}} p_{\mathrm{outlet}} \, dS. \tag{1}$$

With the normalization of the drag force by the dynamic pressure and the vehicle's frontal area $A = 2.02\ \mathrm{m}^2$, the instantaneous drag coefficient $C_d(t)$ can be calculated as:

$$C_d(t) = \frac{D(t)}{\frac{1}{2}\rho(\overline{u_{env}} - u_{\mathrm{car}})^2 A}. \tag{2}$$

While the inlet pressure term can be neglected, since the static in-plane pressure equals the environmental pressure ($p_{inlet} = p_\infty$), the outlet pressure term in equation 1 could only be neglected if the outlet plane for the control volume approach is chosen far away (5 characteristic length scales, according to Terra et al. (2017)) such that the pressure has recovered to the static pressure of the environment. To calculate the outlet pressure, the Pressure Poisson equation from van Oudheusden (2013) is implemented, under the assumption that incompressible flow conditions are present.

Starting from the momentum equation with the known fluid density ρ and viscosity μ, where $\mathbf{u}$ is the instantaneous velocity, p the instantaneous pressure:

$$\nabla p = -\rho\frac{D\mathbf{u}}{Dt} + \mu\nabla^2\mathbf{u} \tag{3}$$

The material acceleration can be rewritten from an Eulerian perspective:

$$\frac{D\mathbf{u}}{Dt} = \frac{\partial\mathbf{u}}{\partial t} + (\mathbf{u}\cdot\nabla)\mathbf{u} \tag{4}$$

Taking the divergence from equation 3, the pressure field can be computed as:

$$\nabla\cdot(\nabla p) = \nabla\cdot(-\rho\frac{D\mathbf{u}}{Dt} + \mu\nabla^2\mathbf{u}) \tag{5}$$

Assuming that the flow incompressible, thus divergence free $\nabla\cdot\mathbf{u} = 0$, equation 4 can be substituted in equation 5 resulting in:

$$\nabla^2 p = -\rho\nabla\cdot(\mathbf{u}\cdot\nabla)\mathbf{u} \tag{6}$$

Notice that, in the derivation of equation (6), the viscous contribution is neglected according to deKat and van (2012) due to the high Reynolds number of the flow. Additionally, the assumption is made that the flow is sufficiently 2D in order to apply the 2D-Pressure Poisson equation and equation 5 can be written in Cartesian form, in order to calculate the pressure gradient from in-plane velocity and van Oudheusden (2013):

$$\frac{\partial^2 p}{\partial y^2} + \frac{\partial^2 p}{\partial z^2} = \rho\left\{(\frac{\partial v}{\partial y})^2 + 2\frac{\partial w}{\partial y}\frac{\partial v}{\partial z} + (\frac{\partial w}{\partial z})^2\right\} \tag{7}$$

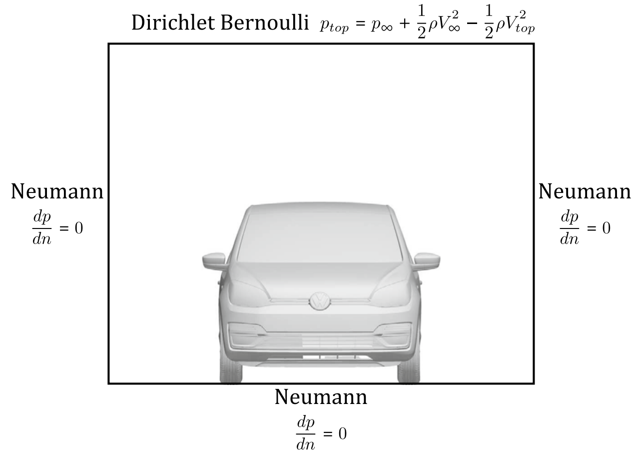

Fig. 8 Boundary conditions for pressure poisson equation

In order to solve the partial differential equation 7, the four boundary conditions displayed in Fig. 8 are implemented.

3.4 Numerical simulations

In order to compare the experimental data to CFD simulations, two different numerical setup approaches for the two regions of interest were carried out.

Ring of fire street simulation—Wake flow A spalart–allmaras delayed detached eddy simulation (DDES) is carried out using OpenFOAM's semi-implicit method for pressure–velocity coupling, i.e., the PIMPLE algorithm. The methodology is originally developed by Islam (2009). The total simulation time covers 4 s physical time, whereby the mean flow quantities are averaged after an initial transient of 2 s. This setup takes the simplified geometries of the experiment into account, where a tunnel with the same dimensions shown in Fig. 1 with a flat roof including the side barriers and the ground are specified as a *translatingWallVelocity* boundary condition. The mesh is a hexahedra-based mesh created by snappyHexMesh generated from triangulated car surface geometry (STL format). It consists of 123 million cells which are clustered close to the car body and in regions were high flow velocity gradients are expected. To keep the cell count within reasonable limits, standard wall functions are applied to model viscous effects in the near-wall region.

Aero-acoustic simulation—mirror & A-pillar flow Aero-acoustic simulations are conducted for the investigation of the flow around the side mirror. The numerical setup is similar to that described above but with an enlarged virtual wind tunnel layout consisting of around 150 million cells to reduce blockage effects. Due to the much finer resolution around the mirror surface, improved delayed detached Eddy simulation (IDDES) turbulence modeling is used to avoid artificial flow separations on the mirror housing and to capture the relevant physics. The total simulation time covers 1.317 s physical time whereby the mean flow quantities are averaged over the interval [1.0; 1.317] s.

4 Results

The following chapter gives an overview on the PIV results from the two regions mirror and wake and the comparison to the numerical data. Coordinates are displayed in the vehicle coordinate system (see Fig. 3) and are normalized to the vehicle height $h = 1.47\ m$. The corresponding mean velocities $\overline{u}, \overline{v}, \overline{w}$ are normalized to the car's velocity of $u_{car} = 33.33$ m/s. The presented results are based on a limited number of runs, thus only demonstrating the proposed methodology.

4.1 Mirror region

The flow field on the area of the A-pillar and mirror is compared to a state of the art IDDES simulation explained in 3.4.

The resulting mean stream wise velocity $\overline{u}$ shows good accordance to the numerical data, even though the limited number of 32 phase-averaged experimental runs limits a statistically significant comparison. Due to the fact that the experiments were conducted during the night, the car's headlights could not be switched off (Volkswagen safety regulations prohibits switching off the headlights on the test track) nor could the preprocessing eliminate all the light, thus resulting in a small error at the location where the headlights were behind the laser sheet and captured by the cameras, see Fig. 9. Furthermore, the measured surrounding velocity (at $\frac{y}{h} < -0.6$) at the front of the car at $z/h = 0$ and $z/h = 0.25$ is significantly lower than in the simulation, due to head wind of approximately $1 - 3$m/s during the experiments.

Further downstream, the difference between experimental and numerical results decreases and the shear layer at the A-pillar as well as the stagnation in front of the mirror is very well captured by the experimental data.

The inhomogeneous seeding distribution for each run and the relative thick light sheet have an effect on the correlation-based evaluation, as mentioned in Sect. 3.2, which results in additional noise. It also should be noted that the u-velocity is only reconstructed by the v and w components and the stereoscopic angle of cameras 3 and 4 was limited to $\alpha = 23°$. This small angle leads to a larger error in the out-of-plane component (Prasad 2000). For further analysis, the three velocity components $(\overline{u}, \overline{v}, \overline{w})$ are extracted along x/h at a stagnation point of the side mirror (red cross in Fig. 10 right) for both the experimental data and the simulation. The before-mentioned higher noise/error in the $\overline{u}$-component can also be noted here, especially compared to the $\overline{w}$-component which has the lowest error, since the cameras were mounted on top of each other. It is clearly noticeable that the experimental data is in good accordance with the simulation up to the stagnation at $x/h = 0.78$ with differences of velocity not exceeding 10 % of u_{car}. The highly turbulent flow in the wake of the mirror $(x/h > 1.1)$ results in erroneous PIV calculation which is attributed to low seeding density and high out-of-plane velocity in this region, yielding high fluctuations. Thus, the current correlation-based approach should not be used in such regions with high turbulence in combination with low seeding density and a relative thick light sheet.

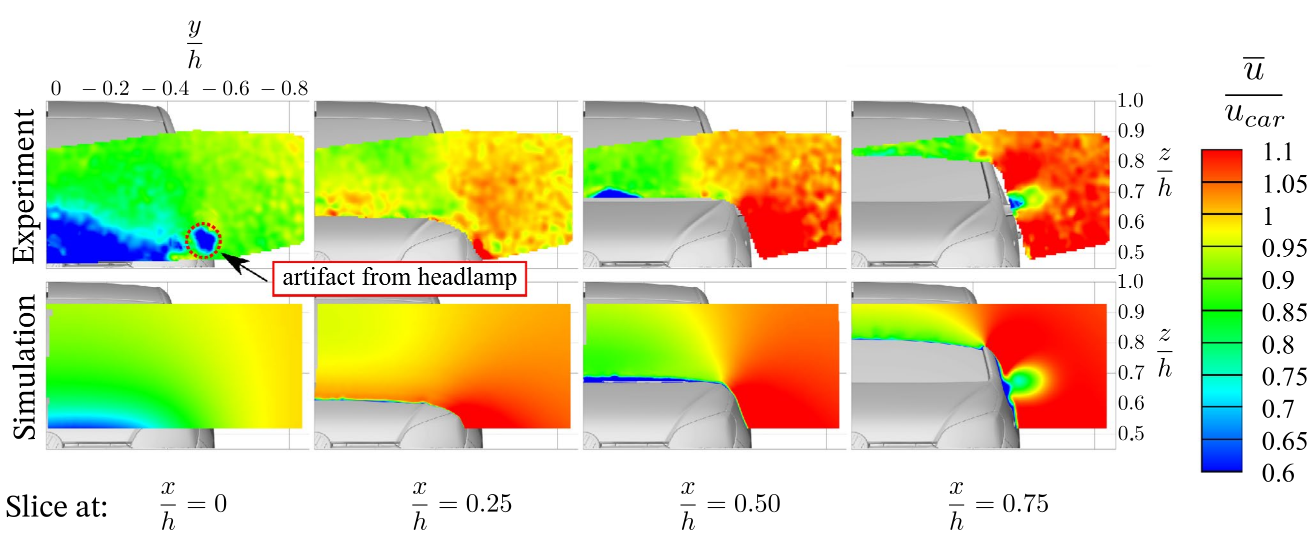

Fig. 9 Comparison of A-Pillar and mirror flow field: dimensionless streamwise mean velocity $\frac{\overline{u}}{u_{car}}$; top: experimental results (average of 22 runs); bottom: numerical simulation

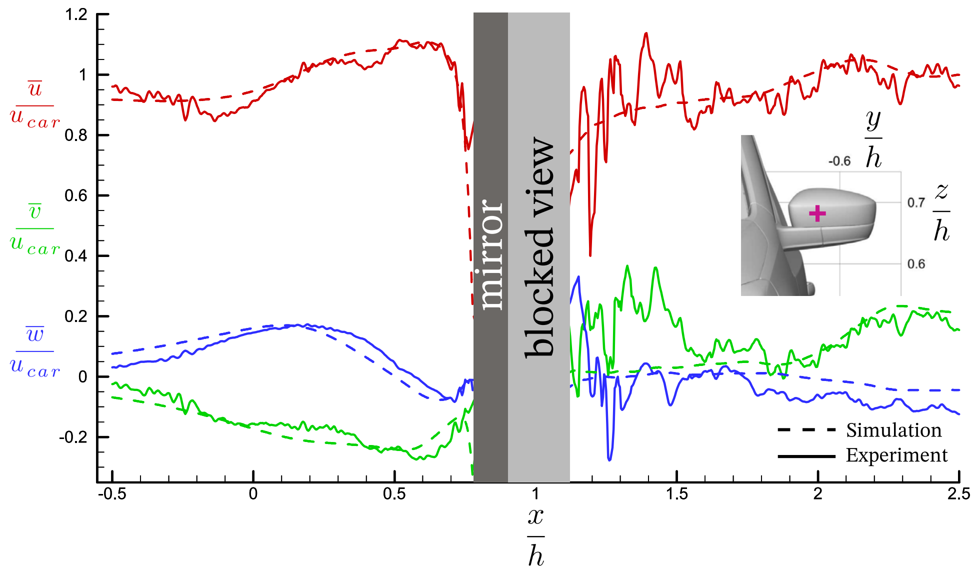

Fig. 10 Dimensionless mean velocities $\frac{\overline{u}}{u_{car}}$; $\frac{\overline{v}}{u_{car}}$; $\frac{\overline{w}}{u_{car}}$ along x/h at $y/h = -0.56$, $z/h = 0.68$

4.2 Wake flow

In this section, the PIV results (phase-average of 22 runs) of the wake flow of the Volkswagen up! will be compared to the Ring of Fire street simulation explained in Sect. 3.4. The experimental data is transformed as described in Sect. 4.1 and additionally the wake distance x_w is introduced with $x_w = 0$ m at the back of the car. The wake contour and the in-plane velocity vector components are shown in Fig. 11.

The low pressure in the near wake at $x_w = 0.5$ m, thus a distinct suction from the outside of the wake region toward the center, is clearly resolved, with a decreasing effect with further distances, thus a lower magnitude of the in-plane vectors outside the wake region. The clear upwash in the center of the wake at $x_w = 0.5$ m and $x_w = 1.0$ m, as a result of the suction from the sides and underneath the car is clearly resolved by the experiment, showing very good accordance to the simulation results.

At $x_w = 0.5$ m, the wake features a trapezoidal shape, with its bottom edge, having an extent of approximately 1 h, larger than its top edge. The velocity deficit inside the wake exceeds $\overline{u}/u_{car} = -0.2$. Two counter-rotating vortices are present around z/h = 0.6, symmetrically with respect to y/h = 0. These vortices induce an upwash at the middle of the wake and an inwash from the sides, thus squeezing the wake laterally. The presence of these vortices is still clear at $x_w = 1.0\,m$, where the velocity deficit reduces to $\overline{u}/u_{car} = -0.1$. Further downstream, two counter-rotating vortices appear close to the ground (z/h < 0.25), which annihilate the top vortices and induce a downwash at the middle of the wake. Due to the injection of air into the wake from the sides, the wake recovers quickly, with a maximum velocity deficit of 0.4 at $x_w = 3\,m$. The shape of the wake contour shows in all streamwise distances good agreement to the numerical results.

Taking a look at the bottom of the flow field, it can be noted that the experimental data differs to the simulation, mainly due to reflections of the laser light on the ground and a sparse seeding density, leading to insufficient image quality to determine particle displacement. Furthermore, the mesh refinement in the vicinity of the car and especially at the ground boundary may also have an effect on the simulated flow field in those regions.

Moreover, it can be noted that the wake flow fields of the experiment have less data at negative y/h-direction, which can be explained by the lateral shift of 10 – 20 cm for each run, due to the lack of an automated positioning of the car. The averaging of the different runs therefore led to slight cut off of the resulting velocity field at the left side.

A comparison of the experimental and the simulation data at different slices behind the car is shown in Fig. 12. Overall the agreement between simulations and PIV is good, with both approaches predicting similar velocity deficits at the different downstream distances. The root-mean-square difference between PIV and CFD results reaches values of 9.7 %, 9.2 %, 7.6 % & 7.0 % at wake distances of 0.5 m, 1.0 m, 2.0 m & 3.0 m, respectively. However, small differences can be noticed; in particular, the PIV profiles exhibit some oscillations which are ascribed to the limited statistical convergence (only 22 runs were used for the average due to limitations in the measurement time) and the noise in the measurements.

At x_w=0.5 m, it can be noted that the streamwise velocity is not totally resolved by the experiments (Fig. 12a) green line) which can be explained by the lack of sufficient seeding density in this low-pressure region. Further downstream, in the wake this effect decreases, whereas

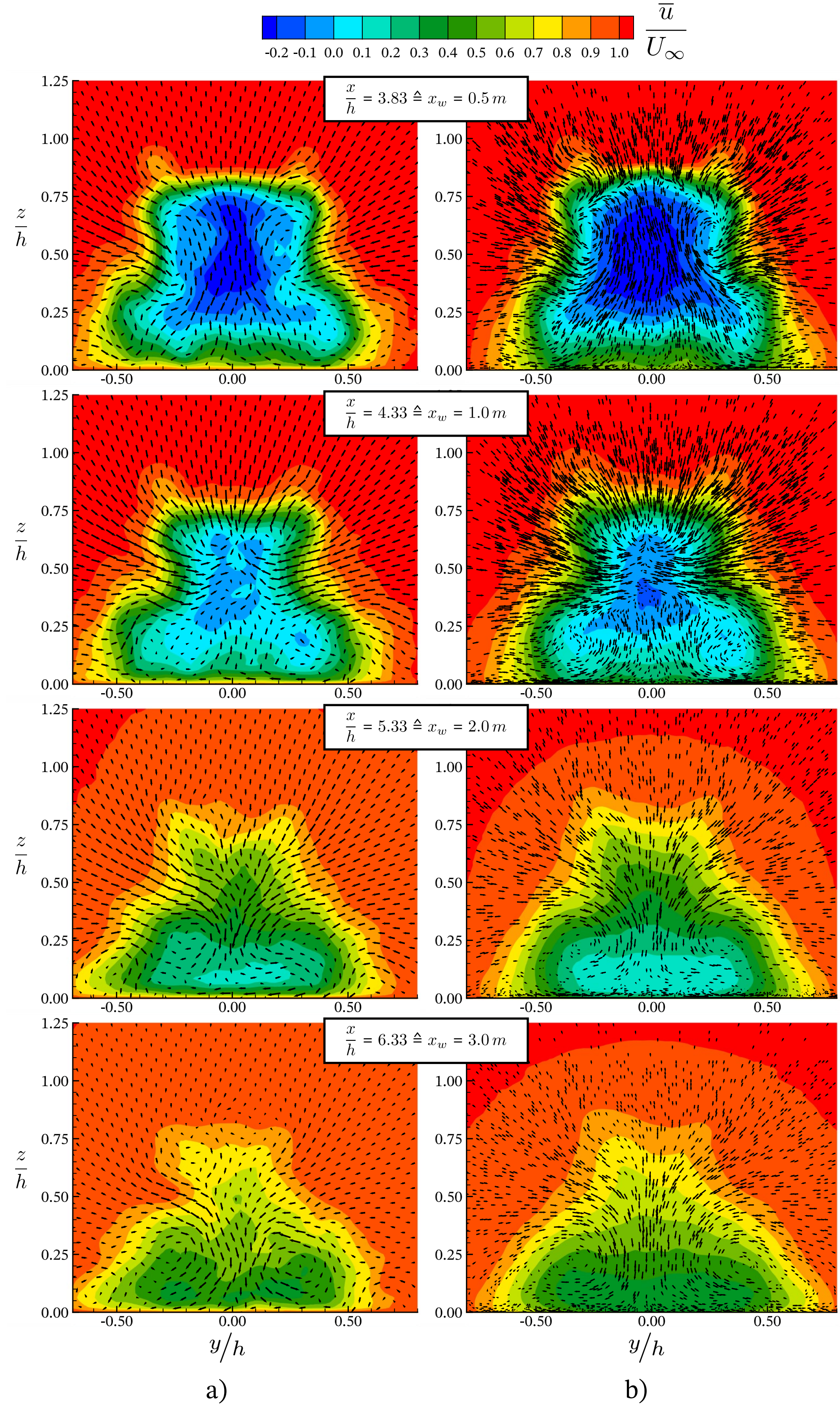

Fig. 11 Volkswagen up! wake contour of streamwise mean velocity $\frac{\overline{u}}{U_\infty}$ at wake distances x_w = 0.5m,1.0 m, 2.0 m, 3.0 m. **a** Experimental and **b** numerical results

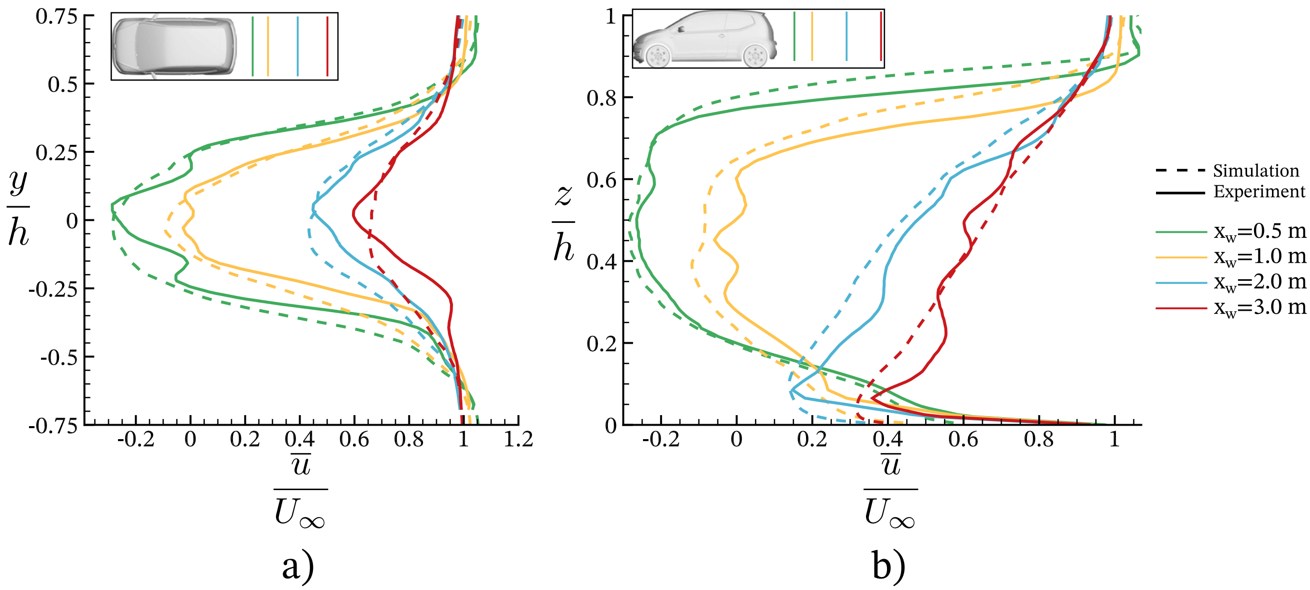

Fig. 12 Volkswagen up! comparison of mean streamwise velocity in the wake. **a** y-Slice at z/h=0.5; **b** z-slice at y/h=0

the highly turbulent flow and the averaging of only 22 runs can be an explanation of the higher noise levels in the experimental data. Due to the limited seeding density and in turn spatial resolution of the measurements, the boundary layer close to the ground can only be resolved reliably up to z/h=0.08 (approximately 0.12 m).

4.3 Aerodynamic drag evaluation

For the drag calculation, the momentum approach in Sect. 3.3 was applied to the experimentally obtained velocity fields at wake distances x_w {1; 1.5; 2; 2.5; 3; 3.5; 4; 5} m. In order to reduce the standard deviation of the drag calculation, for each run, the inlet flow velocity was calculated from the average of 100 fields 1 s before the passage of the car, whereas the instantaneous velocity field of each run was considered for the outlet plane. The drag results are shown in Fig. 13. Up to a distance of x_w=1.5 m, the drag value is underestimated as compared to the wind tunnel result, probably due to the highly turbulent flow and the large out-of-plane component in the near wake of the car. Thus, the pressure cannot be calculated accurately by the 2D-Pressure Poisson equation in this region. In the wake distance 2–3m, the mean drag reaches a nearly constant value and decreases afterward for all three configurations. The reason for the drag decrease at larger streamwise distance

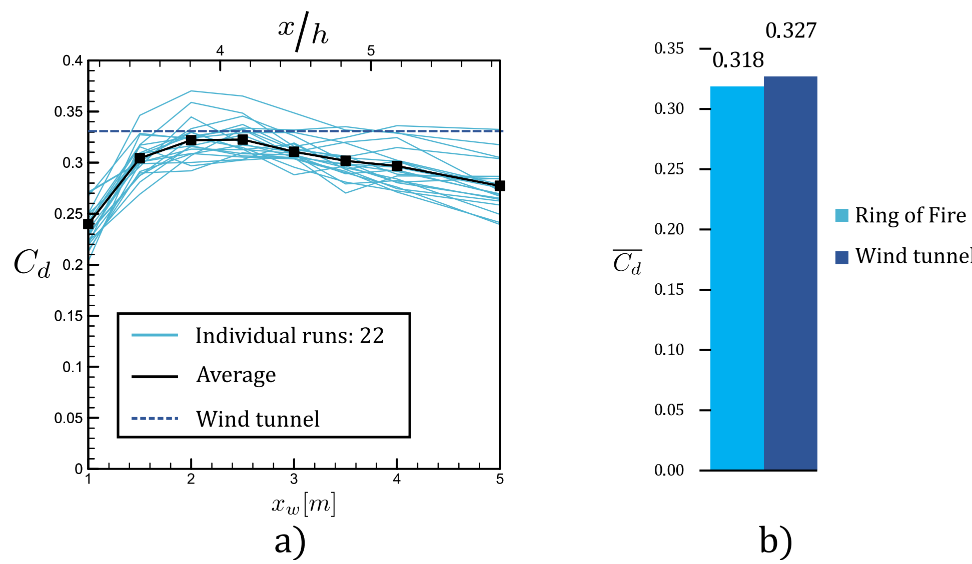

Fig. 13 Drag results Volkswagen up! **a** in wake distance x_w from 1 to 5 m; **b** mean drag comparison to windtunnel

is twofold: on the one hand, part of the wake exits the field of view, hence less momentum deficit is measured. On the other hand, the wake interacts with the stationary ground, hence it dissipates part of its momentum. To evaluate the proposed method, the calculated drag, obtained by averaging the C_d results in the range $2\ m \leq x_w \leq 3\ m$, is compared to the mean drag resulting from wind tunnel measurements of the test vehicle by Schmitz (2017), that were performed in the aeroacoustic wind tunnel of Audi AG equipped with a six-component balance. A detailed description of the wind tunnel is given by Wickern and Lindener (2000). Overall, the drag calculation from PIV data by means of the momentum approach shows good accordance to standard wind tunnel measurements with a relative error below 3

5 Conclusion

The world-first large-scale particle image velocimetry measurements for on-road flow quantification of car aerodynamics were performed on a test track. The nonintrusive measurements principle was applied by means of a helium-filled soap bubbles flow tracers and high-speed image acquisition. The Stereo-PIV results of two different regions (wake and mirror) illustrate the capability of the Ring of Fire concept to resolve the flow topology of car aerodynamics at conventional driving speeds. Resulting vector fields can be used to validate numerical simulations if a significant number of runs are recorded and provide deeper information of on-road flow phenomena. Especially the capability to measure on-road flow phenomena like body ground interaction, the flow field of rotating wheels or also vehicles in platoon is pointed out. Another advantage of the system is flexibility of the setup, thus different configuration of the cars geometry can be measured very easily.

Moreover, the drag calculation from PIV data by means of the momentum approach shows, with only limited number of experimental runs, good accordance to standard wind tunnel measurements (relative difference below 3 %). Further improvements could involve the use of 3D-pressure data from volumetric particle tracking approaches as shown by Hüttig et al. (2023). Also, the influence of ambient flows on the accumulation of seeding particles in the measurement volume needs to be addressed in future experiments, for instance, by a longer tunnel and industrial air curtains at the entrance and exit. For a more efficient use of the large number of seeding particles, the use of multiple PIV setups or complete volumetric data acquisition should be considered.

Appendix A: Additional experimental data

See Fig. 14.

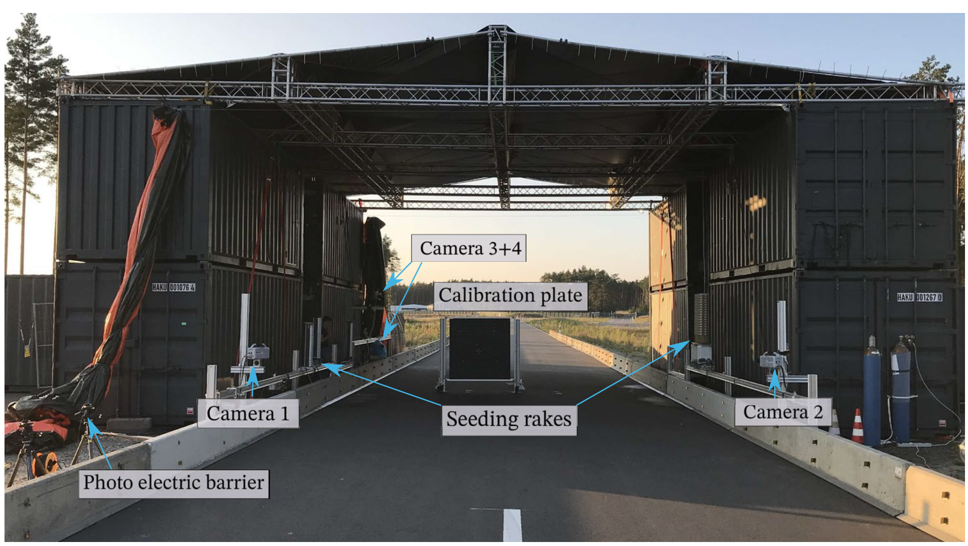

Fig. 14 Experimental setup

Supplementary Information The online version contains supplementary material available at https://doi.org/10.1007/s00348-025-04025-w.

Acknowledgements The authors would like to thank Steffen Kroll, Paul Bernicke and Saad Kamran (Volkswagen AG) for providing the CFD results and also Uwe Dierksheide and Dirk Michaelis from LaVision GmbH for their support during the experiments. Furthermore, financial support of the Hamburg University of Applied Sciences is acknowledged. The Technical University Braunschweig is acknowledged for providing the Volkswagen up!.

Author contributions SH, MK, TG and GB performed the experiments. SH, MK and GB analyzed the data. SH prepared figures and wrote the manuscript. AS and RA supervised the experiments and analysis, reviewed the results and edited the manuscript. All authors reviewed the manuscript.

Funding Open Access funding enabled and organized by Projekt DEAL.

Data availability The data that supports the findings of this study cannot be made publicly available due to confidentiality reasons. Supplementary movies are available on the online version.

Declarations

Conflict of interest The authors have no Conflict of interest as defined by Springer, or other interests that might be perceived to influence the results and/or discussion reported in this paper.

References

Beresh S, Neal D, Sciacchitano A (2021) Validation of Multi-Frame PIV Image Interrogation Algorithms in the Spectral Domain, 14th International Symposium on Particle Image Velocimetry, Vol.1 No.1 https://ispiv21.library.iit.edu/index.php/ISPIV/article/view/63/71

Bosbach J, Kühn M, Wagner C (2009) Large scale particle image velocimetry with helium filled soap bubbles. Exp Fluids 46:539–547. https://doi.org/10.1007/s00348-008-0579-0

Dawi AH, Akkermans RAD (2018) Spurious noise in direct noise computation with a finite volume method for automotive applications. Int J Heat Fluid Flow 79:243–256. https://doi.org/10.1016/j.ijheatfluidflow.2018.06.008

deKat R, van Oudheusden BW, (2012) Instantaneous planar pressure determination from PIV in turbulent flow. Exp Fluids 52:1089–1106. https://doi.org/10.1007/s00348-011-1237-5

Ebrahim H, Dominy R (2021) The effect of afterbody geometry on passenger vehicles in platoon. Energies 14(22):7553. https://doi.org/10.3390/en14227553

Haff J (2015) A comparative study of engineering tools in heavy vehicle aerodynamics. Dissertation. Technische Universität Ilmenau https://www.db-thueringen.de/receive/dbt_mods_00026088

Haff J, Lange S, Barth T, Wilhelmi H (2017) An Experimental Study of the Underbody Flow of a VW Golf VII Under On-Road and Wind-Tunnel Conditions. Progress in Vehicle Aerodynamics and Thermal Management. FKFS 2017 https://doi.org/10.1007/978-3-319-67822-1_12

Hüttig S, Gericke T, Sciacchitano A, Akkermans RAD (2023) Automotive on-road flow quantification with a large scale Stereo-PIV setup, 15th International Symposium on Particle Image Velocimetry - ISPIV 2023, San Diego - USA http://hdl.handle.net/20.500.12680/5h73q343c

Henning A, Richard H, Kowalski T, Gries T, Huntgeburth S, Loose S (2016) Full-Scale PIV Measurement on High-Speed Trains; 18th International Symposium on Applications of Laser Techniques to Fluid Mechanics, LISBON - PORTUGAL http://ltces.dem.ist.utl.pt/lxlaser/lxlaser2016/finalworks2016/papers/03.12_1_320paper.pdf

Islam M, Decker F, Villiers ED, Jackson A, Ginés J, Grahs T, Gitt-Gehrke A, Font J (2009) Application of Detached-Eddy Simulation for Automotive Aerodynamics Development. SAE Technical Paper 2009-01-0333 https://doi.org/10.4271/2009-01-0333

Jones BM (1936). The Measurement of Profile Drag by the Pitot-traverse Method. Aeronautical Research Committee. Reports and memoranda – no.1688

Jessing C (2021) Charakterisierung instationärer Anströmsituationen und Analyse ihrer Einflüsse auf die Fahrzeugaerodynamik. Dissertation, Wissenschaftliche Reihe Fahrzeugtechnik Universität Stuttgart. https://doi.org/10.1007/978-3-658-34847-2

Keane RD, Adrian RJ (1991) Optimization of particle image velocimeters: II. Multiple pulsed systems. Meas Sci Technol 2(10):963. https://doi.org/10.1088/0957-0233/2/10/013

Kurtulus DF, Scarano F, David L (2007) Unsteady aerodynamic forces estimation on a square cylinder by TR-PIV. Exp Fluids 42:185–196. https://doi.org/10.1007/s00348-006-0228-4

Mohebbian A, Rival DE (2012) Assessment of the derivative-moment transformation method for unsteady-load estimation. Exp Fluids 53:319–330. https://doi.org/10.1007/s00348-012-1290-8

Perry AE (1982) Hot-wire Anemometry. Oxford University Press, Oxford

Placzek R (2018) Active Flow Control for Drag Reduction of a Square-back Car Model. Dissertation. Technische Universität Braunschweig

Prasad A (2000) Stereoscopic particle image velocimetry. Exp Fluids 29:103–116. https://doi.org/10.1007/s003480000143

Schmitz O (2017) Hochaufgelöste Druckmessungen an einem Kraftfahrzeug. Master Thesis. Technische Universität Braunschweig

Schröck D (2012) Eine Methode zur Bestimmung der aerodynamischen Eigenschaften eines Fahrzeuges unter böigem Seitenwind. Dissertation. Universität Stuttgart https://doi.org/10.1007/978-3-658-21545-3

Sciacchitano A, Scarano F, Wieneke B (2012) Multi-frame pyramid correlation for time-resolved PIV. Exp Fluids 53:1087–1105. https://doi.org/10.1007/s00348-012-1345-x

Spoelstra A, de Martino Norante L, Terra W, Sciacchitano A, Scarano F (2018) An assessment of the Ring of Fire approach for indoor and outdoor on-site sports aerodynamic investigation. In Proceedings of the 19th international symposium on application of laser and imaging techniques to fluid mechanics http://www.lisbon-lasersymposium.org/download/?g=CD8D35F1-7413-4C65-BEE6-0CF75E1CED35

Spoelstra A, de Martino Norante L, Terra W, Sciacchitano A, Scarano F (2019) On-site cycling drag analysis with the Ring of Fire. Exp Fluids. https://doi.org/10.1007/s00348-019-2737-y

Spoelstra A, Terra W, Sciacchitano A (2023) On-site aerodynamics investigation of speed skating. J Wind Eng Ind Aerodyn. https://doi.org/10.1016/j.jweia.2023.105457

Spoelstra A, Hirsch M, Sciacchitano A, Scarano F (2021) Uncertainty assessment of the ring of fire concept for on-site aerodynamic drag evaluation. Meas Sci Technol. https://doi.org/10.1088/1361-6501/abb50d

Stoll D (2018) Ein Beitrag zur Untersuchung der aerodynamischen Eigenschaften von Fahrzeugen unter böigem Seitenwind, Dissertation. Wissenschaftliche Reihe Fahrzeugtechnik Universität Stuttgart https://doi.org/10.1007/978-3-658-21545-3_3

Terra W, Sciacchitano A, Scarano F (2017) Aerodynamic drag of a transiting sphere by large-scale tomographic-PIV. Exp Fluids. https://doi.org/10.1007/s00348-017-2331-0

Terra W, Spoelstra A, Sciacchitano A (2023) Aerodynamic benefits of drafting in speed skating: estimates from in-field skater's wakes and wind tunnel measurements. J Wind Eng Industr Aerodyn. https://doi.org/10.1016/j.jweia.2023.105329

van Oudheusden BW (2013) PIV-based pressure measurement. Meas Sci Technol 24:032001. https://doi.org/10.1088/0957-0233/24/3/032001

Watkins S (1990) Windtunnel modelling of vehicle aerodynamics: With emphasis on turbulent wind effects on commercial vehicle drag. Dissertation. Victorian University of Technology https://researchrepository.rmit.edu.au/esploro/outputs/doctoral/Windtunnel-modelling-of-vehicle-aerodynamics/9921861403001341#file-0

Westerweel J, Scarano F (2005) Universal outlier detection for PIV data. Exp Fluids 39:1096–110. https://doi.org/10.1007/s00348-005-0016-6

Wieneke B (2005) Stereo-piv using self-calibration on particle images. Exp Fluids 39:267–280. https://doi.org/10.1007/s00348-005-0962-z

Wickern G, Lindener N, (2000) The Audi Aeroacoustic Wind Tunnel: Final Design and First Operational Experience. SAE Technical Paper 2000-01-0868 https://doi.org/10.4271/2000-01-0868

Authors and Affiliations

Steffen Hüttig[1,2] · Malte Kühn[1] · Timo Gericke[1] · Guus Bloem[3] · Andrea Sciacchitano[3] · Rinie A. D. Akkermans[4]

✉ Steffen Hüttig
steffen.huettig2@volkswagen.de

Timo Gericke
timo.gericke@volkswagen.de

[1] Volkswagen AG, Wolfsburg, Germany

[2] Faculty of Mechanical Engineering, Technische Universität Braunschweig, Braunschweig, Germany

[3] Faculty of Aerospace Engineering, Delft University of Technology, Delft, The Netherlands

[4] Department of Automotive and Aeronautical Engineering, Hamburg University of Applied Sciences, Hamburg, Germany